Automatic Statistical Volume Element modeling based on the Unified Topology Model

Adrien Couture[a,b], Vincent François[b], Jean-Christophe Cuillière[b,*], Philippe Pilvin[a]

[a] *IRDL, Université de Bretagne-Sud, France*

[b] *ERICCA, Université du Québec à Trois-Rivières, Québec, Canada*

Abstract:

Needs for new particle based heterogeneous materials as led to the development of many Statistical Volume Element (SVE) modeling schemes tailored to specific shapes of particles or meshing procedures. To generalize the numerical analysis of particle filled SVEs, a modeling methodology based on the Unified Topology Model (UTM) is proposed. Using the concept of Boundary Representation (BRep) and a modified Random Sequential Adsorption (RSA) algorithm, the geometry of a Statistical Volume Element (SVE) can be generated automatically with any shape of particles. Using an integration of Computer-Aided Design (CAD) and mesh tools, a mesh size map is constructed with the objective of minimizing the number of mesh elements while preserving quality of the discretization. The SVE is meshed using proven CAD model meshing algorithms for a robust and reliable result. Simulation and post processing are carried out automatically, without any user interaction. To illustrate the potential of this new method, a short glass fiber / epoxy matrix composite is modeled with spherical and elongated cylindrical particles.

Keywords:

Statistical Volume Element (SVE), Unified Topology Model (UTM), Computer-Aided Design (CAD), Finite element Analysis (FEA), Homogenization

1. Introduction

Understanding the mechanical behavior of a given randomly oriented inclusion based composite material can be a tedious process. Even when mechanical properties of individual constituents are fully understood and their shapes and sizes quantified, their combined interaction and the process by which they are bounded together can produce a material of unknown properties. Actual mechanical testing requires numerous steps ranging from samples fabrication to calibrated testing and in some cases can be near to impossible to accomplish due to the size or nature of the required samples [1]. Hence, the quest for predicting the material properties, which would yield faster prototyping and faster decision making has resulted in a variety of analytical and numerical modeling schemes. Analytical models can give a fair overview of the mechanical modulus in cases where the contrast between the different constituents is low but these models lack the ability to take into account the size, geometry, and distribution of the constituents. On the other hand, numerical models such as the Finite Element Analysis (FEA) of the Statistical Volume Element (SVE) have shown great interest in the research community for its ability to represent and simulate a numerical representation of a heterogeneous material. In this paper, the term SVE is used instead of the Representative Volume Element (RVE) as different realization of SVE are expected to have different averaged values which differs from the uniqueness of the RVE (Fig. 1). Such an approach must be employed when the size of a RVE is too large to be numerically evaluated. The biggest challenge of this method is obtaining a realistic representation of the material's microstructure. As illustrated by many research papers, the mechanical properties of a simulated composite material can be influenced by the constituent's shape [2-5], orientation [2, 6, 7], volume fraction [7, 8] and distribution [9, 10]. The size of the SVE and the number of realizations can also impede the realism and statistical accuracy of the numerical model [4, 8, 11-17]. Large SVEs will require significant computing power but will provide a more accurate estimation whereas smaller SVEs are individually less accurate but, if taken in a larger number, can provide a statistically representative estimation of the material mechanical behavior. A numerical SVE can be obtained from an actual composite sample via a scanning process [18-21]. A numerical SVE can also be generated based on predetermined experimental parameters. The main advantage of generating SVEs over sample-based methods is the fact that it does not require physical samples. One can generate, simulate and compile mechanical properties of a theoretical composite without actually manufacturing samples of this composite. Using this approach over a range of material formulations can provide an early on insight of the optimal material which reduces prototyping time and costs.
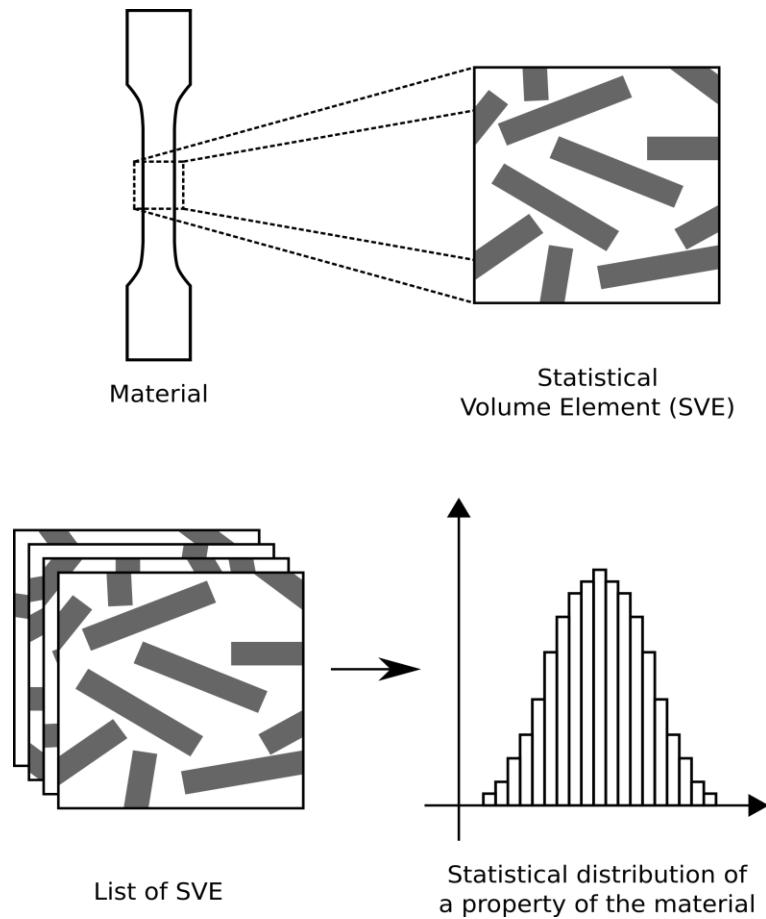
Fig. 1. Illustration of the SVE modeling approach. Multiple SVEs are randomly generated according to the material's microstructure. The SVEs are numerically studied and their properties combined to form a statistical description of the simulated material.

The first step towards generating a SVE is creating its geometrical representation. Early studies showed SVE filled with spherical particles positioned using the Random Sequential Adsorption (RSA) algorithm [1-3, 5, 8, 22-24]. Using spherical particles allows for simple interference detection during the addition of each particle. Interference detection is heavily used in the RSA method and is one of the many challenges of packing particles. Later studies presented improved version of the RSA algorithm using different geometric overlap detection algorithms based on the shape's parametric equations. These extensions of the RSA algorithm enable using ellipsoids [2, 4, 23-27] and cylinders [2, 7, 15, 17, 24, 27-31] as particles. Convex polyhedral shapes have also been used with the RSA algorithm by computing the intersection of planar faces [3, 5]. More recent studies presented molecular dynamic based SVE generation methods [32-34]. The advantage of molecular dynamic based SVE generation methods is their ability to attain higher volume fractions than with the RSA algorithm. Even though the complexity of

particles shapes has evolved over time, the final geometric representation of a SVE is still mainly composed of lists of elementary shapes with limited use of Computer-Aided Design (CAD) tools. For example, a SVE filled with spherical particles can be geometrically defined by a list of analytical spherical surfaces. These representations can be efficient and easily implemented but they tend to be limited to a particular SVE type. The meshing process follows the same trend. Generated SVE are either meshed with unstructured mesh generation methods (Delaunay, advancing front, octree [35]) using, in most cases, quadratic tetrahedrons [2, 5, 8] and hexahedrons [36] or with structured voxel based mesh generation methods [4]. The main advantage of using an unstructured mesh generation method over a voxel-based method is its ability to better fit curvilinear geometry. A voxel mesh needs to be dense enough to realistically depict a curved shape without significant chopping effect. If well optimized, an unstructured mesh can feature fewer nodes than an equivalent structured voxel-based mesh, which results in a lighter system. The main difficulty in using these unstructured mesh generation techniques with the above-mentioned geometric representation is the lack of a generalized mesh generation procedure. Automatic mesh generation procedures from CAD models are well known and documented [35]. Without using a proper CAD representation of SVEs, meshing each type of SVE requires using specific meshing procedures. Thus, any addition or modification to the geometrical representation of a SVE requires setting up new meshing procedures.

In order to study efficiently and accurately multiple types of inclusion-based materials, the methodology by which SVEs are generated, meshed, simulated and homogenized must be generalized and automated. The aim of this study is to propose a new approach towards automatically generating and modeling SVEs. This new approach is based on the Unified Topology Model (UTM) [37], a model whose objective is to closely integrate Computer Aided Design (CAD) with Finite element Analysis (FEA). The UTM uses the concept of Boundary Representation (BREP), which is a classical CAD geometric data structure that involves and integrates two types of information: topological information and geometrical information. All modern CAD software use BREP for modelling complex parts. When using BREP, a volumetric part is defined as a volume which is itself defined as a closed envelope. This envelope is defined as a list of faces. A face is defined using an underlying surface which is bounded by a closed loop. Each loop is composed of a list of edges. Finally, an edge is defined using an underlying curve, which is bounded by two vertices and each vertex is associated with an underlying point along with its coordinates (Fig. 2).
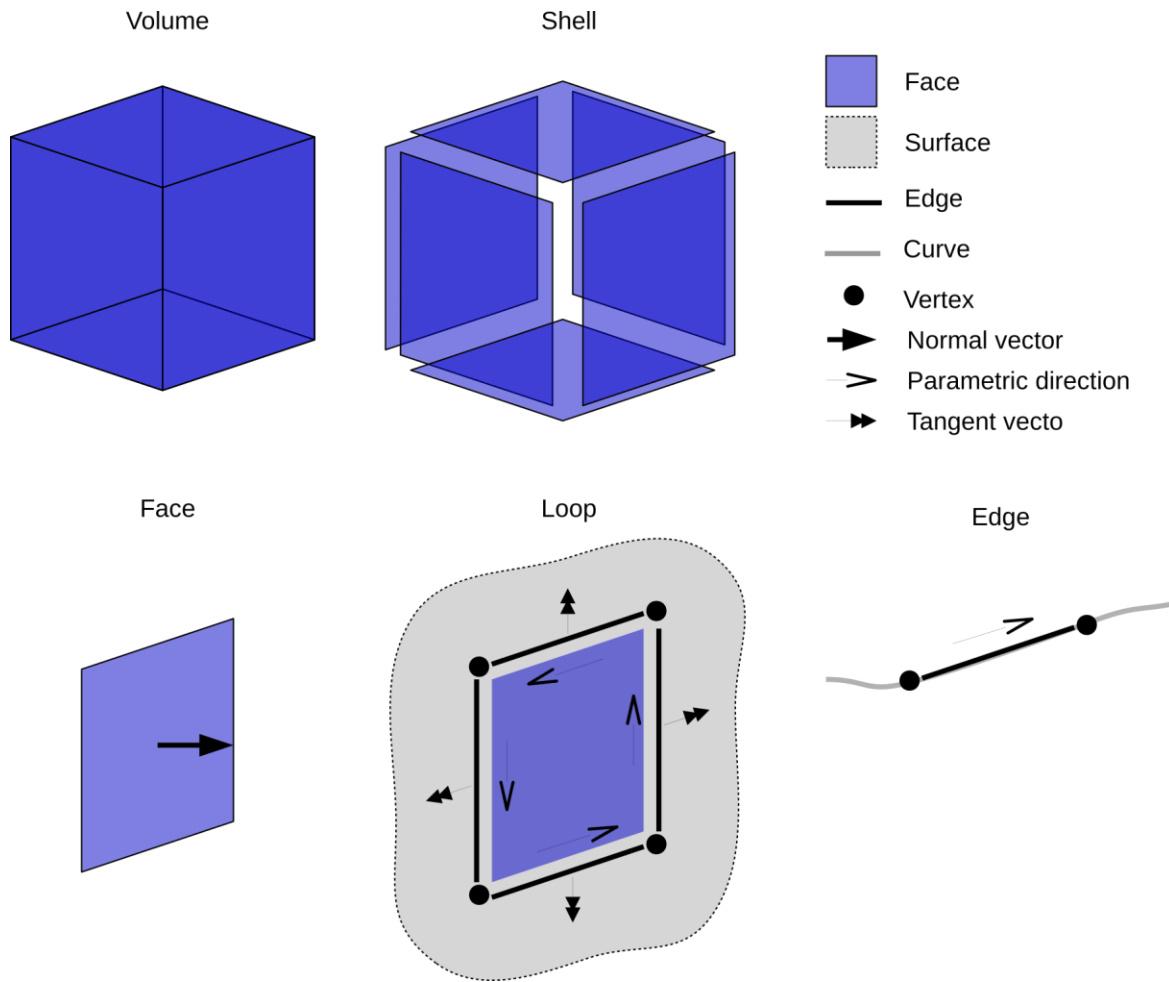
Fig. 2. Illustration of the BREP model.

Topological information relates to data arrangement whereas geometrical information provides a mathematical definition of surfaces, edges and vertices in a BREP structure. One key feature of the UTM is that it avoids topological redundancy through the use of co-topological entities. For example, if two volumes share a common face, this face is only defined once and the orientation of each volume face is kept valid with the use of two co-faces. Each co-face corresponds to one of the two volumes in contact. Thus, a co-face can be seen as a common face between two volumes along with the addition of a normal orientation vector. This normal vector defines on which side of the common face is located the material of the co-face associated volume (Fig. 3). Consequently, as illustrated in Fig. 3, normal vectors of the two co-faces associated with the two volumes in contact, are always oriented in opposite directions. These two co-faces are usually referred to as *partner co-faces*. In a similar way, the concept of co-topological entities also includes co-edges and co-vertices. A volumetric part is thus defined as a closed envelope containing a list of co-faces, a co-face itself defined by a face and so on.
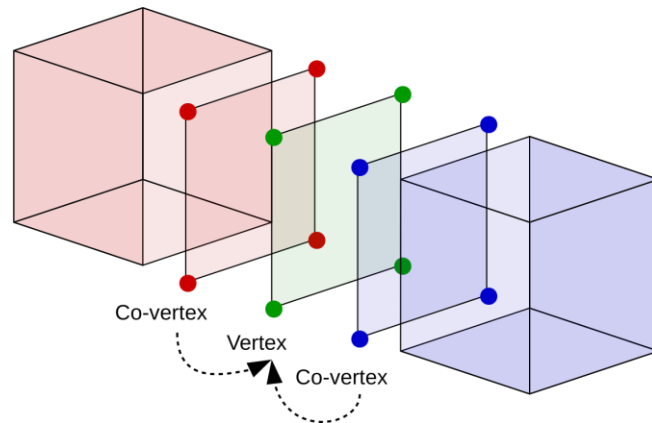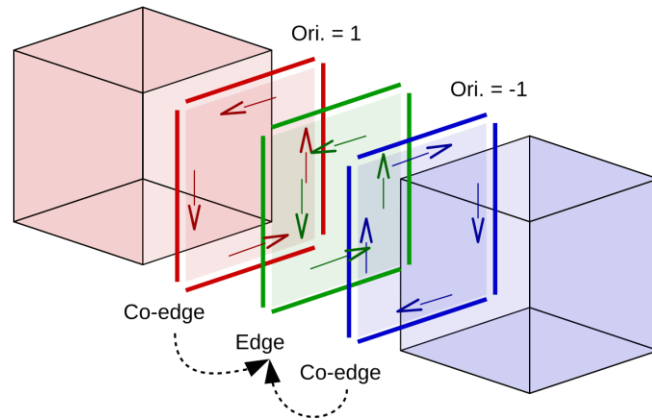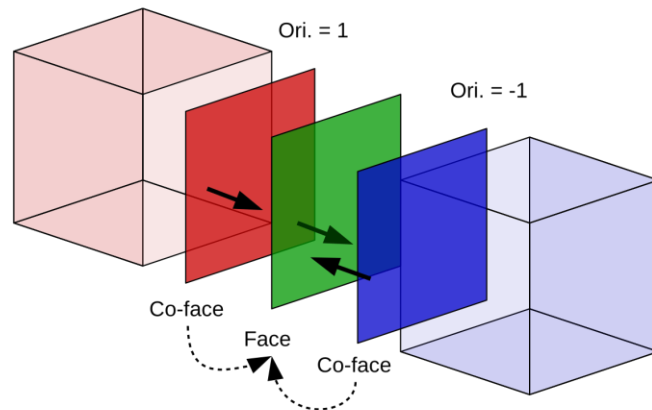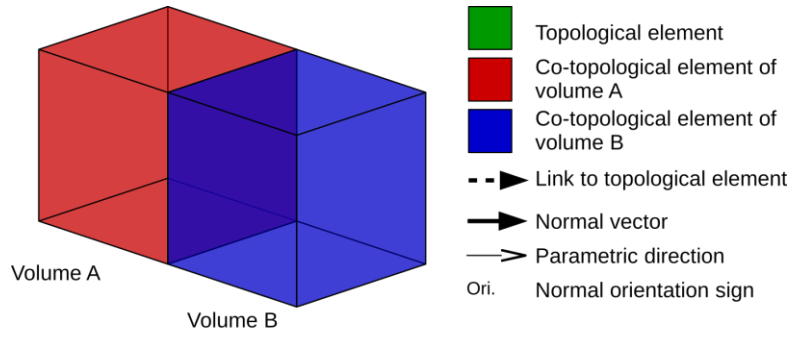
Fig. 3. Illustration of the co-topology concept.

The UTM is not limited to specific CAD and FEA software. The UTM can link itself with different CAD software by encapsulating its functionalities based on open source libraries or Application Programming Interfaces (APIs). Therefore, using the UTM, a programmer can construct algorithms using CAD functionalities without rewriting every line of code when a change of CAD software occurs. The same principles apply to the integration of FEA in the UTM. CAD-FEA integration relies on a bidirectional link between the BREP topological entities and the mesh entities (FEA nodes, edges, faces and elements). With this link, one can apply boundary conditions directly on topological entities without any preexisting mesh. During automatic mesh generation, each mesh entity is linked to its corresponding topological entity. Before the FEA simulation itself, node groups and element groups are automatically created and transmitted to the FEA software considered. Once FEA is completed, results are imported back to the UTM. This allows using CAD and meshing tools for post-processing FEA results. Automation provided by the UTM has been successfully applied to many research fields such as topology optimization [38], fixtureless inspection [39] and automatic a priori mesh adaptation [40].

The following sections will provide an in-depth description of a methodology aimed at automatically modeling a SVE, which is based on the UTM. The process by which the CAD representation of a SVE is obtained using an adapted RSA algorithm is discussed in section 2. Automatic application of boundary conditions and material properties to BREP topological entities is described in section 3. Section 4 details how a mesh size map is automatically defined using geometric tools and a structured grid. Linear and quadratic tetrahedral mesh generation is described in section 5. The homogenization process is detailed in section 6. Finally, results obtained from short glass/epoxy composite SVEs modeled with spheres and cylinders are presented and discussed in section 7. The paper ends with a conclusion and perspectives of future work in Section 8.

2. Automatic CAD generation of Statistical Volume Elements

Fast, efficient and automatic generation of CAD models associated with Statistical Volume Elements (SVEs) is a key step in the methodology presented in this paper, since a large number of SVEs have to be considered. The underlying CAD modeler used in this implementation of the UTM is Open Cascade™ [41]. This modeler is open-source which enables a direct access to its geometric modeling tools. CAD models of SVEs are automatically generated using classical Boolean operators (union, subtract, intersection) along with a parent operator, which will be referred to as the *fragmentation operator*.

The fragmentation operator is internally implemented and used in commercial CAD software but it is usually inaccessible for users. The fragmentation operator acts before union, difference or intersection operators by defining the new boundaries between the objects (Fig. 4).
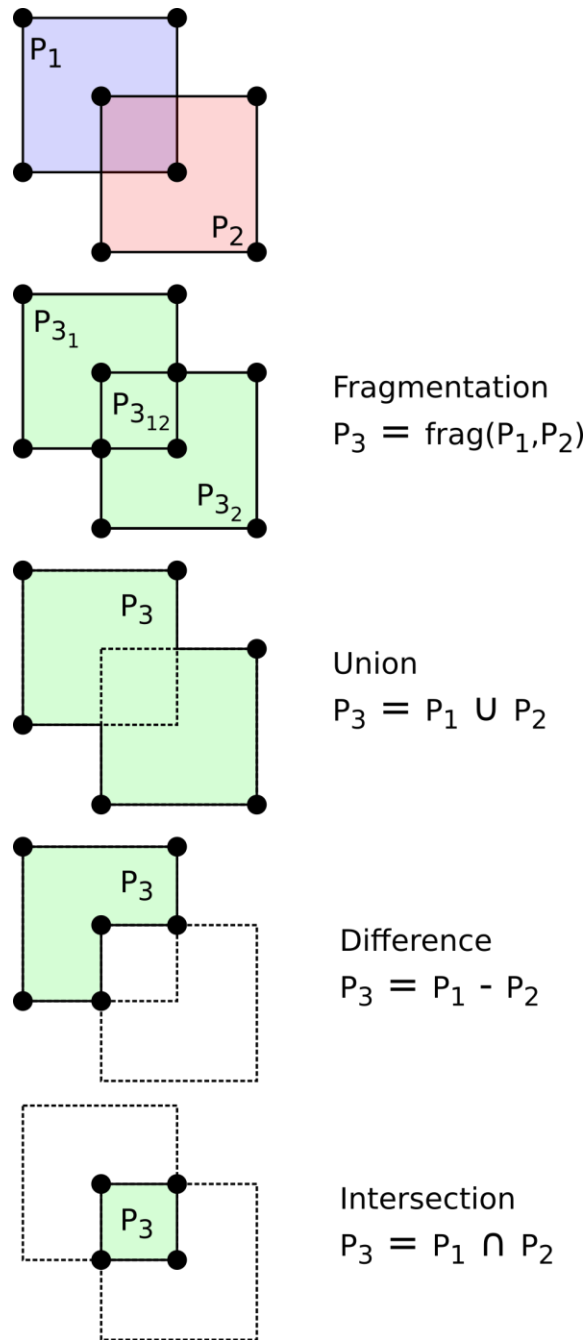

Fig. 4. Illustration of the fragmentation operator and derived Boolean operators.

This process enables using co-topological entities. When two topological entities are associated with the same underling geometrical entity, two co-topological entities are created, each containing the respective orientation of associated topological entities. One of the two topological entities is kept while the other is discarded and the two newly created co-topological entities are linked to the remaining topological entity. This concept is illustrated in figure 3. When volume A is generated, the face (green) in contact with volume B is created and a co-face (blue) is created and linked to it. When volume B is generated, the face in contact with volume A is discarded, and a co-face (red) is linked to the green face. The blue co-face has the same orientation as the green face and the blue co-face the opposite so as to maintain the correct orientation. Hence, the boundary shared between to volumes is only represented by one topological entity.

In this work, the RSA algorithm is used to randomly generate the CAD model of a SVE. RSA algorithm relies on gradually inserting particles in the SVE until reaching a target volume fraction and on detecting geometrical overlap between a candidate particle and previously inserted particles. Detecting overlap of a given particle requires rapidly identifying nearby particles, which can be efficiently performed using a *search grid* (Figure 6). In this work, the search grid used is composed of a regular grid of hexahedral cells, covering the area of the SVE. A particle is linked to each cell that intersects its bounding box.

Generating the CAD model of a SVE starts with generating a cube which represents the empty matrix. This cube is then modified through gradual insertion of particles inside it. Orientation, location and shape of these particles can be generated randomly or with imposed values. A particle that intersects boundaries of the SVE must be over a minimum volume, its faces over a minimum area and its edges over a minimum length to avoid generating small or distorted elements. Particles that are inserted inside the SVE must be sufficiently far away from boundaries of the SVE and sufficiently far away from each other so not to generate too small or distorted mesh elements. Also, angles between two faces must be large enough to avoid generating flat finite elements. The following algorithm summarizes the major steps of our implementation of the RSA algorithm (Algo 1). List 1 defines the corresponding variables. Figure 5 shows the resulting BREP model of two SVEs (one filled with spheres and one filled with cylinders). As a first approach, we did not consider periodic conditions (or constraints) in this work to simplify the development of the different methods presented. We could apply periodic conditions with the approach presented in this paper, given that the RSA algorithm can be adapted towards generating periodic CAD representations. A new particle could be created with its corresponding periodic counterparts and the assessment of intersections would have to be applied to both the new particle and its periodic

counterparts. In this work, we used a classical version of the RSA algorithm, which has some limitations when trying to reach high volume fractions. Enhancements of the RSA algorithm have been proposed in the literature to reach higher volume fractions, notably by coupling the RSA algorithm with a particle rearrangement algorithm [22].

List 1. Variables for the RSA algorithm

| Variable	Definition
V_f	Current volume fraction
$V_{f_{target}}$	Volume fraction target
$Dist_{min}$	Minimum allowable distance between two topological entities
Vol_{min}	Minimum allowable volume for a volume entity
$Area_{min}$	Minimum allowable area for a face entity
$Length_{min}$	Minimum allowable length for an edge entity
$Angle_{min}$	Minimum allowable angle between two face entities
Nb_{step}	Number of parametric discretization steps
M_{struct}	CAD model of the SVE
C	SVE cubic geometry
P	Particle geometry
G_P	Particle search grid
L_P	List of neighboring particles
$Dist_{P_i,P_j}$	Minimal distance between P_i and P_j
$Dist_{P,C}$	Minimal distance between P and borders of C
$Inter_{P,C}$	Intersection Boolean operator on P and C
$Frag_{P,C}$	Fragmentation operator on P and C
t	Parametric variable of a curve

1 RSA algorithm

Data: Position distribution, orientation distribution, type of geometry, $V_{f_{target}}$, $Dist_{min}$, Vol_{min}, $Area_{min}$, $Length_{min}$, $Angle_{min}$, Nb_{step}

**Result:** CAD model of microstructure M_{struct}

1 Create RVE cube C

2 Create particle search grid G_P

3 **while** $V_f < V_{f_{target}}$ **do**

4   Generate position and orientation[random or fixed] (x, y, z), (ϕ, θ)

5   Generate particle geometry P [random or fixed] at (x, y, z) and (ϕ, θ)

6   List neighboring particles L_P with search grid G_P

7   **foreach** $P_i \in L_P$ **do**

8   Get min. distance $Dist_{P,P_i}$ between P and P_i

9   **if** $Dist_{P,P_i} < Dist_{min}$ **then** reject P

10   Detect intersection $Inter_{P,C}$ of P with C

11   **if** $Inter_{P,C}$ *is true* **then**

12   Generate intersection P_{inter} between P and C

13   Get volume $Vol_{P_{inter}}$ of P_{inter}

14   **if** $Vol_{P_{inter}} < Vol_{min}$ **then** reject P

15   **foreach** $Face_i \in P_{inter}$ **do**

16   Get area $Area_{Face_i}$ of $Face_i$

17   **if** $Area_{Face_i} < Area_{min}$ **then** reject P

18   **foreach** $Edge_i \in P_{inter}$ **do**

19   Get length $Length_{Edge_i}$ of $Edge_i$

20   **if** $Length_{Edge_i} < Length_{min}$ **then** reject P

21 $P = P_{inter}$

22   **else**

23   Get min. distance $Dist_{P,C}$ between P and C

24   **if** $Dist_{P,C} < Dist_{min}$ **then** reject P

25   Generate fragmentation between P and C: P_{frag} and C_{frag}

26   **if** $Inter_{P,C}$ *is true* **then**

27   **foreach** $Edge_i \in P_{frag}$ **do**

28   **for** $t = t_{min}$ **to** t_{max} **step** $(t_{max} - t_{min})/Nb_{step}$ **do**

29   **foreach** $Pair \{Face_i, Face_j\} \in Edge_i$ **do**

30   Get angle $Angle_{i,j}$ between $\{Face_i, Face_j\}$ at t

31   **if** $Angle_{i,j} < Angle_{min}$ **then** reject P, P_{frag}, C, C_{frag}

32 $C = C_{frag}$

33   Add P to G_P

34   Update V_f

35   Add P to M_{struct}

36 Add C to M_{struct}

a)

b)
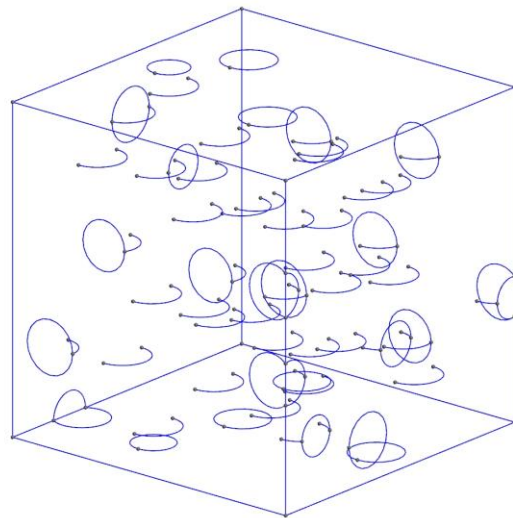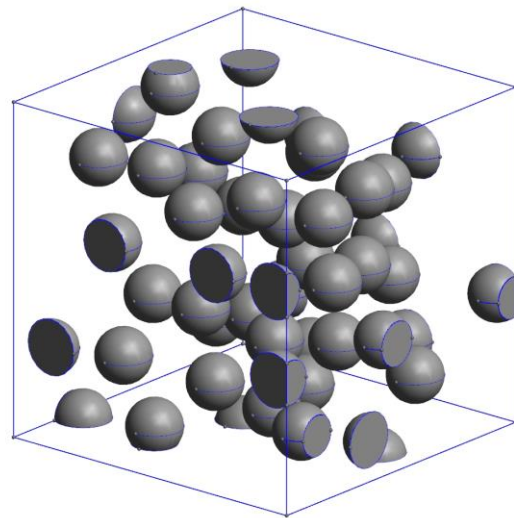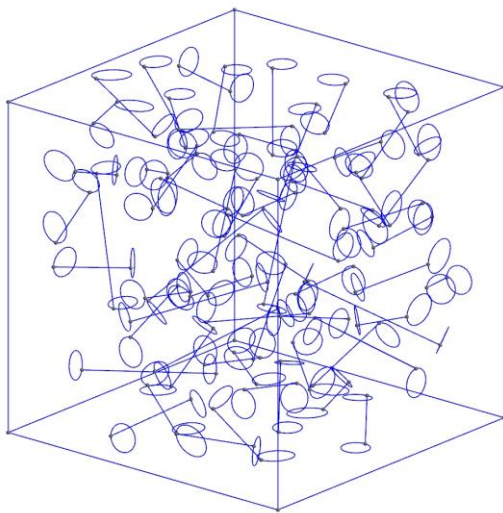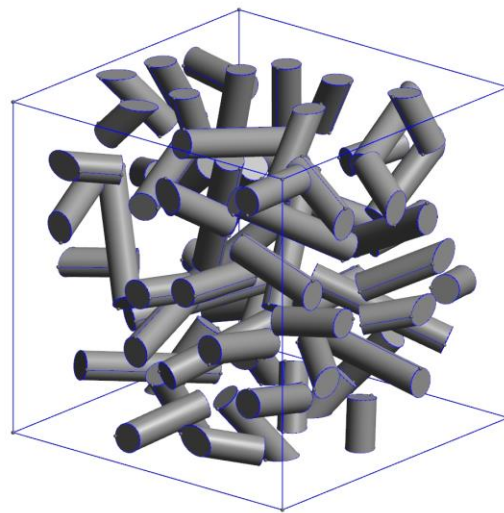
Fig. 5. BREP model of an SVE with 10% (volume fraction) of spherical particles (S1FV10) (a) and cylindrical particles (C1FV10) (b). BREP edges (left), BREP faces (right)

Fig. 6. Illustration of the search grid used for the proximity detection. a) Search grid containing previously inserted particles (blue). b) New particle (red). c) Each cell in contact with the bounding box of the new particle is listed (gray). d) Proximity detection of the green particle.

Data associated with CAD include: number of particles, statistical analysis on the size of particles, volume fraction of each constituents and orientation tensor in the case of elongated particles. For elongated particles such as cylinders or ellipsoids, t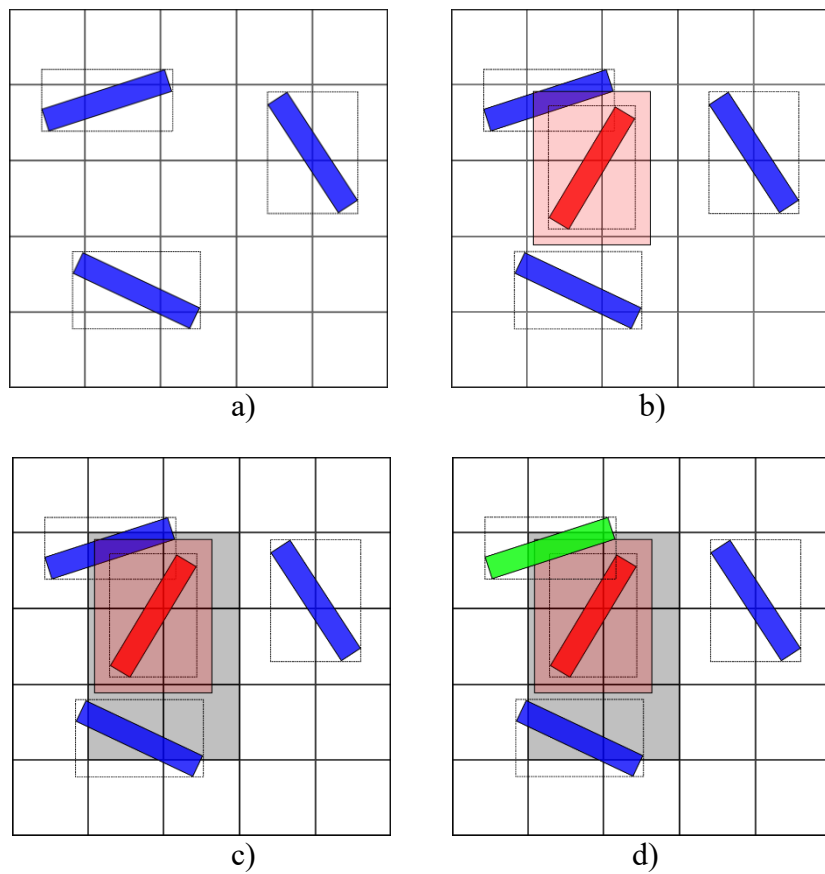he orientation tensor is based on the orientation vector of particles (EQ 1-2), as described in [42]. This tensor provides information about isotropy in the distribution of particles orientation.

$$
\begin{aligned}
p_x &= sin\,\theta\,cos\,\varphi \\
p_y &= sin\,\theta\,sin\,\varphi \\
p_z &= cos\,\theta
\end{aligned}
\qquad (1)
$$

$$
\underline{\underline{a_2}} = \langle \underline{p} \otimes \underline{p} \rangle \qquad (2)
$$

3. Material properties and Boundary conditions

Materials properties can be randomly generated based on an imposed distribution or using fixed values. Material properties are associated with volumetric topological entities. Using the link between topological entities and associated mesh elements provided by the UTM model, materials properties will subsequently be transferred to these mesh elements in the FEA model. Boundary conditions are also applied on topological entities of the BREP. In this case, they are automatically applied on the six planes of the cube. In this work, Kinematic Uniform Boundary Conditions (KUBC) (EQ 3) and Static Uniform Boundary Conditions (SUBC) (EQ 4) are used to model the mechanical response of isotropically distributed inclusion filled SVEs. KUBC consist in applying a uniform displacement vector on the SVE's boundary and SUBC in applying a uniform stress vector on the SVE's boundary. Two types of load cases are used to evaluate the mechanical response of the material: a hydrostatic load and a deviatoric load. The use of four load cases (non-zero components: hydrostatic KUBC $E_{11} = E_{22} = E_{33} = \varepsilon$, deviatoric KUBC $E_{12} = E_{13} = E_{23} = \varepsilon$, hydrostatic SUBC $\Sigma_{11} = \Sigma_{22} = \Sigma_{33} = \sigma$, deviatoric SUBC $\Sigma_{12} = \Sigma_{13} = \Sigma_{23} = \sigma$) instead of 12 linearly independent cases is motivated by a significant reduction in computation time and by the assumption of a macroscopically isotropic composite.

$$
\underline{u}(\underline{x}) = \underline{\underline{E}} \cdot \underline{x} \quad \forall \underline{x} \in \partial V \qquad (3)
$$

$$
\underline{t}(\underline{x}) = \underline{\underline{\Sigma}} \cdot \underline{n} \quad \forall \underline{x} \in \partial V \qquad (4)
$$

4. Automatic generation of a mesh size map

A finite element mesh size distribution, referred to as a mesh size map is imposed and plays a key role in the process. Indeed, it allows minimizing the number of mesh elements in areas where particles are far from each other and it also ensures that mesh quality is preserved in areas where particles are close to each other or close to the SVE boundaries by refining the mesh in these areas. In this work, a mesh size map is represented as a scalar field $\mathcal{M}(x, y, z)$. Definition of this field first involves a nominal mesh element size E_n, which is imposed in areas where the mesh doesn't need to be refined. In refinement areas, $\mathcal{M}(x, y, z)$ is generated in order to ensure a minimum number of mesh elements layers between two topological entities (referred to as Nb_{ele}) and to impose a specific element size (referred to as E_{inter}) at the interface between each particle and the matrix. So, the size map algorithm automatically calculates the local size of mesh elements based on the minimum number of elements layers (Nb_{ele}) required between two distinct topological entities, which is user specified. To insure convergence of advancing front mesh generation, at least two layers of elements ($Nb_{ele} = 2$) must be generated between two neighboring particles or between a particle and SVE boundaries. In this paper, $Nb_{ele} = 2$ has been considered for all results presented. Using more than two layers of elements between close entities improves the local quality of elements but also increases computational time. Studying the effect, on results obtained, of using more than two layers of elements in these locations and looking for the best compromise between accuracy and computational time could be an interesting perspective for future work.

As explained and illustrated in figure 7 and figure 8, this size map is practically defined and interpolated on a regular hexahedral grid covering the entire SVE volume. This regular grid is only used as support for definition of the size map, which is represented as an interpolated size field across the grid cells. Using CAD tools, a constant size value is first calculated and associated with each cell of this grid. Then this mesh size distribution is smoothed and interpolated across the grid. The following algorithm details this mesh size map generation (Algo 2) and List 2 defines its variables. Figure 7 illustrates the three main steps of the algorithm while figure 8 show the resulting size map of a cylinder filled SVE. As explained just above, at this point of our work, the size map calculation algorithm used is an "a priori" refinement algorithm, which means that it calculates the desired size of mesh elements before doing any FEA calculations. In this work, the objective of the mesh size map algorithm is to ensure convergence of the mesh generation process and to promote generating elements with good quality. Further work could be

done towards taking into account singularities and mesh pre-optimization [40] could be employed in this direction to further improve the accuracy of FEA results. "A posteriori" mesh adaptation based on error estimation could also be used to improve this accuracy.

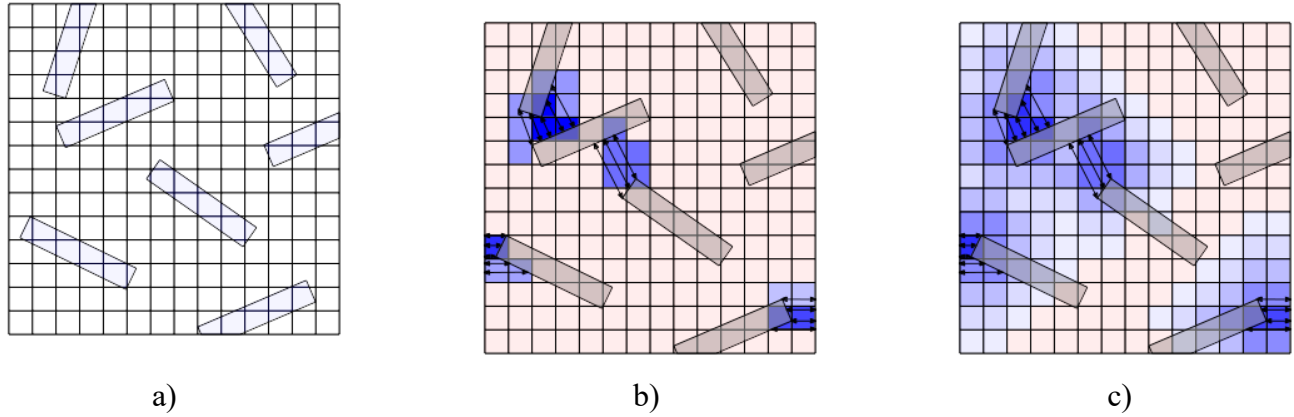a)   b)   c)

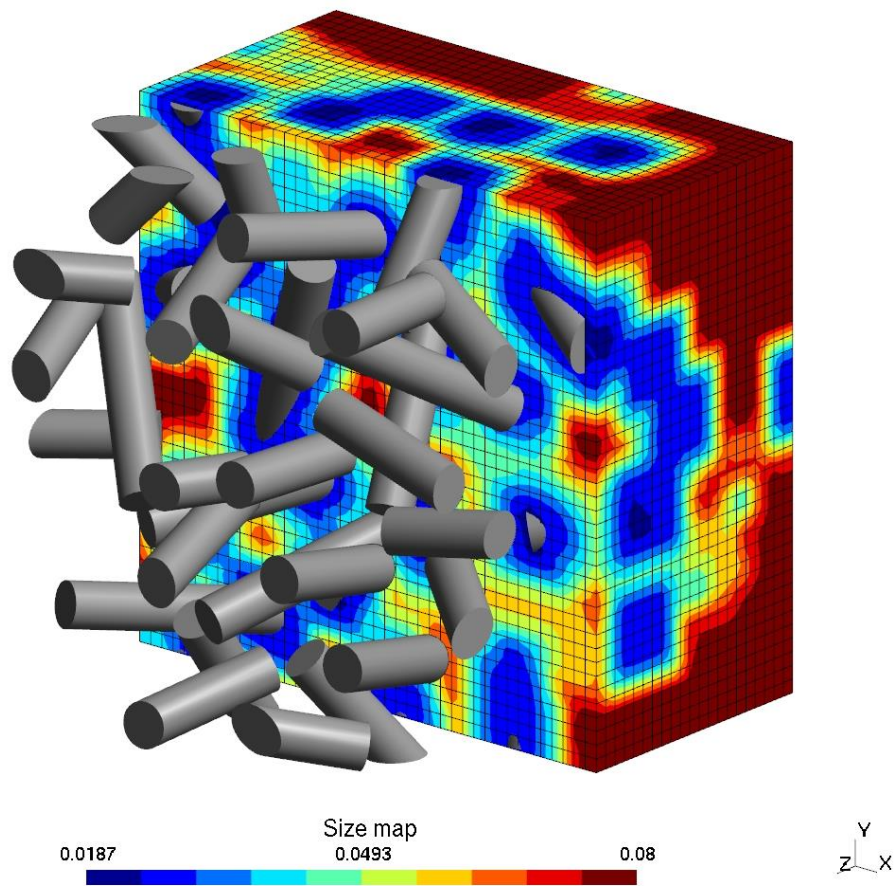Fig. 7. Illustration of the size map algorithm; a) Hexahedral mesh, b) Refinement, c) Smoothing

Size map
0.0187   0.0493   0.08

Fig. 8. Size map for C1FV10

List 2. Variables for the size map algorithm

Variable	Definition
M_{struct}	CAD model of the SVE
E_n	Nominal mesh element size
E_{inter}	Mesh element size at the interface of a volume entity
E_{loc}	Local mesh element size
$E_{average}$	Local average mesh element size
Nb_{ele}	Number of elements between two topological entities
n_x, n_y, n_z	Number of regular hexahedral cells in x, y, z
Nb_{step}	Number of parametric discretization steps
f	Element size increase factor
$\mathcal{M}$	Size map
$\mathcal{T}$	Hexahedral mesh covering $\mathcal{M}$
K	Hexahedral cell
T	Topological entity
G_K	Hexahedral cell search grid filled with $\mathcal{T}$
G_T	Topological entities search grid filled with M_{struct}
L_T	List of neighboring topological entities
L_K	List of neighboring hexahedral cells
$Dist_{T_i,T_j}$	Minimal distance between T_i and T_j
O_K	Sorted array of hexahedral cells
N	Node element

2   Size map construction algorithm

Data: M_{struct}, E_n, E_{inter}, Nb_{ele}, n_x, n_y, n_z, Nb_{step}, f
Result: Size map $\mathcal{M}$

1 Create hexahedral mesh $\mathcal{T}$ covering M_{struct} with n_x, n_y, n_z regular hexahedral cells
2 foreach *Hex. cell $K_i \in \mathcal{T}$* **do** Change element value $E_K = E_n$
3 Create hex. cell search grid G_K filled with $\mathcal{T}$
4 Create topological element search grid G_T filled with M_{struct}
5 foreach $T_{ele} \in M_{struct}$ **do**
6   List neighboring topological element L_T with G_T
7   **foreach** $T_i \in L_T$ **do**
8   **if** T_i *is T_{ele} or $T_i \in T_{ele}$* **then next**
9   Get min. distance $Dist_{T_i,T_{ele}}$ between T_i and T_{ele}
10   **if** $Dist_{T_i,T_{ele}}/E_n > Nb_{ele}$ **then next**
11   **for** *position Pos_i on T_i by parametric sweep of edge, face with Nb_{step} or vertex* **do**
12   Get position Pos_j by nearest projection of Pos_i on T_{ele}
13   List hex cells L_K crossed by vector $\overline{Pos_i, Pos_j}$ with G_K
14   Get local mesh element size $E_{loc} = ||\overline{Pos_i, Pos_j}||/Nb_{ele}$
15   **foreach** $K_i \in L_K$ **do**
16   **if** $E_{loc} < E_{K_i}$ **then** $E_{K_i} = E_{loc}$

17 if $E_{inter} < E_n$ **then**
18   **foreach** $Face_i \in M_{struct}$ **do**
19   List neighboring hex. cells L_K crossed by $Face_i$ with G_K
20   **foreach** $K_i \in L_K$ **do**
21   **if** $E_{inter} < E_{K_i}$ **then** $E_{K_i} = E_{inter}$

22 Create sorted array of hex. cells O_K based on E_K with $\mathcal{T}$
23 while O_K *is not empty* **do**
24   Remove hex. cell K_{min} with min. element size value E_{min} from O_K
25 $E_f = E_{min} \cdot f$
26   **if** $E_f > E_n$ **then next**
27   List hex. cell L_K connected with K_{min}
28   **foreach** $K_i \in L_K$ **do**
29   **if** $E_{K_i} > E_f$ **then**
30 $E_{K_i} = E_f$
31   Add K_i to O_K

32 foreach *Node $N \in \mathcal{T}$* **do**
33   List hex. cells L_K connected with N
34   Get average element size value $E_{average}$ of L_K
35   Change node value E_N to $E_{average}$

5. Automatic mesh generation of Statistical Volume Elements

FE linear mesh elements are automatically generated with respect to the imposed mesh size map above-mentioned. Once generated, each mesh element is linked to its underlying topological entity in the BREP model. At first, mesh nodes are created on BREP vertices, then each BREP edge is discretized with segments [43]. BREP faces are then automatically triangulated using an advancing front mesh generation method [44] and finally, each volume is automatically filled with linear tetrahedrons using a 3D advancing front mesh generation method [37]. Figure 9 illustrates the discretization of BREP edges and faces for the two SVEs introduced in Fig. 5.
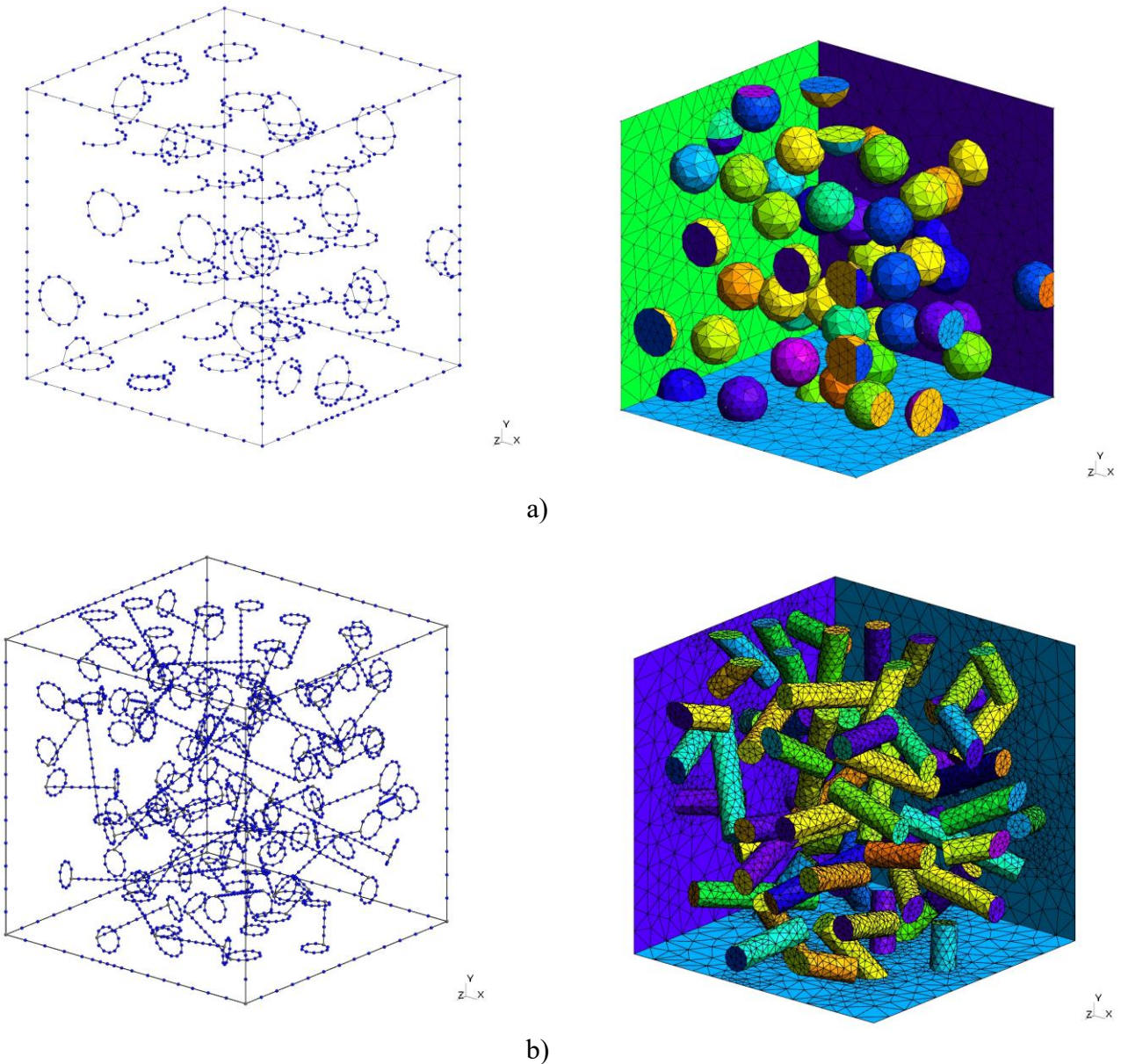

a)

b)

Fig. 9. Linear mesh for S1FV10 (a), C1FV10 (b). Edges discretization (left), Faces discretization (right)

Obtaining accurate FEA results require using quadratic tetrahedrons. Thus, quadratic mesh tetrahedrons are created from previously generated linear mesh elements. Mesh nodes are first inserted in the middle of linear mesh segments. Then, each middle node belonging to a curved BREP geometrical entity (BREP surface or curve) is projected on this entity (surface or curve) so that curvilinear distances between the middle node and end nodes of the curvilinear mesh segment are equal (Fig. 10). In some cases, local geometric configurations of curved entities induce quadratic tetrahedrons with a negative Jacobian, which invalidates these mesh elements. Avoiding quadratic elements with negative Jacobians has been an important subject of interest in the mesh generation community and many solutions have been published over the years [45-47]. In our work, it has usually been observed that less than 0.1% of quadratic tetrahedrons are affected with a negative Jacobian. In this work, a simple node relocation method can be used to solve negative Jacobian mesh configurations. For a negative Jacobian mesh element, each node that had been projected on a curved topological entity is gradually brought back to its initial position until Jacobian turns positive. Although simple, this method proves to be suitable and particularly efficient in our case, as it will be demonstrated in section 7. A comparison between linear and quadratic meshes for a given case is illustrated in figure 11.
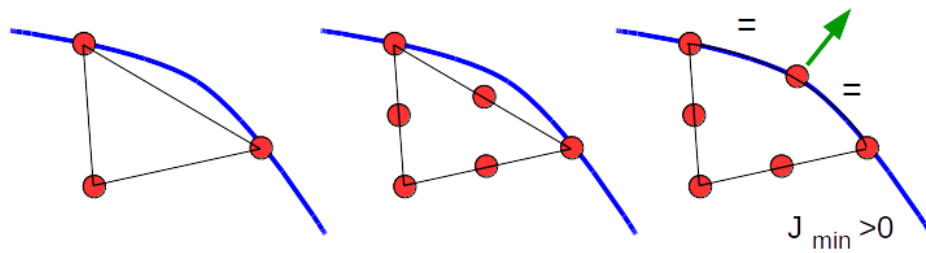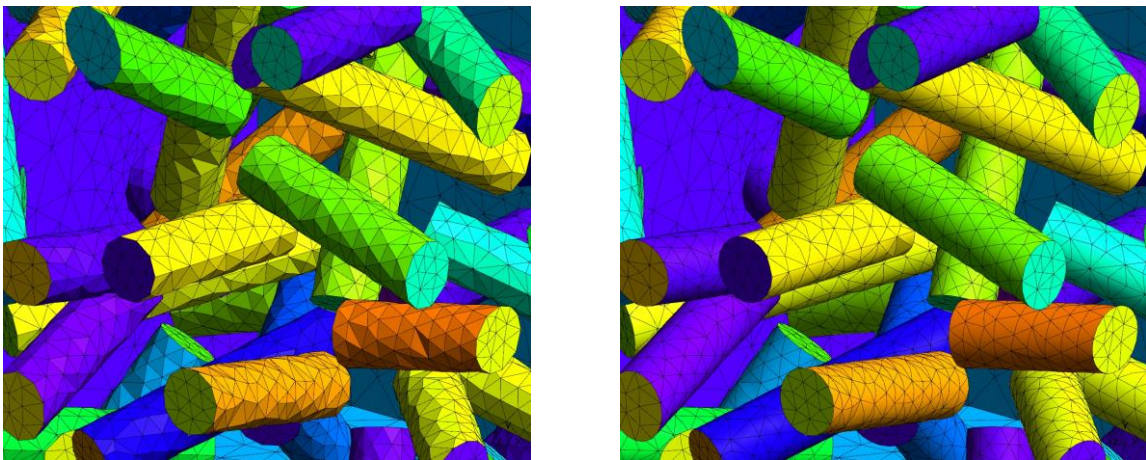

Fig. 10. Middle node relocation

Fig. 11. Comparison between linear (left) and quadratic (right) meshes

Data associated with mesh generation include: number of mesh elements, statistical analysis of quality of linear mesh elements (EQ 5) and volume fraction of each constituents. In Equation (5), Q_K represents a classical quality indicator used in this work for linear tetrahedrons. Q_K values are between 0 (poorest quality, typically for flat elements) and 1 (regular tetrahedron with 4 equilateral faces). In Equation (5) h_{max} is the length of the longest element segment and r_{insc} is the radius of the tetrahedron's inscribed sphere.

$$Q_K = \frac{2\sqrt{6}r_{insc}}{h_{max}} \qquad (5)$$

As mentioned in section 1, one of the main advantages of using the UTM is the link between the CAD model and the FEA mesh. Using this link, mesh elements associated to any topological entity on which a boundary condition is applied are automatically partitioned for the FEA solver. In this work, Code_Aster™ is used [48] as FEA solver. This software is also open-source and is well documented. Script files are automatically generated, FEA solving is automatically performed and relevant FEA results are automatically extracted for further post-processing.

6. Homogenization

Homogenizations is done using the average values of stress and strain fields components (EQ 6-7) for the complete SVE. Calculations of the apparent shear G_{app} and compressibility K_{app} modulus (EQ 8-9) and subsequently the elastic modulus E_{app} (EQ 10) are done with the assumption of a perfectly isotropic material at the macroscopic scale.

$$\underline{\underline{E}} = \langle \underline{\underline{\varepsilon}} \rangle_V = \frac{1}{V}\int_V \underline{\underline{\varepsilon}}(\underline{x})dV \qquad (6)$$

$$\underline{\underline{\Sigma}} = \langle \underline{\underline{\sigma}} \rangle_V = \frac{1}{V}\int_V \underline{\underline{\sigma}}(\underline{x})dV \qquad (7)$$

$$K^{app} = \frac{1}{3}\left(\frac{\Sigma_{11}+\Sigma_{22}+\Sigma_{33}}{E_{11}+E_{22}+E_{33}}\right) \qquad (8)$$

$$G^{app} = \frac{1}{3}\left(\frac{\Sigma_{12}}{2E_{12}} + \frac{\Sigma_{23}}{2E_{23}} + \frac{\Sigma_{13}}{2E_{13}}\right) \qquad (9)$$

$$E^{app} = \frac{9K^{app}G^{app}}{3K^{app}+G^{app}} \qquad (10)$$

7. Results and discussion

To illustrate the benefits of the above-mentioned methodology, a comparison between a glass fiber / epoxy resin material modeled with spherical and cylindrical inclusions is presented. Material properties and SVE cases are first listed. The homogenization results which are the central motivation of this work are presented and discussed. Finally, an analysis of the CAD and mesh data is put forward to validate the modeling approach.

Material properties of glass fibers and epoxy matrix are listed in table 1. The ratio between elastic moduli of these two materials is more than twenty, which is ideal to illustrate the benefits of numerical simulation over analytical analysis of this composite material. With such a contrast, analytical bounds such as Voigt and Reuss or Hashin-Shtrikman bounds [49-51] are spaced farther apart as the volume fraction of glass fiber increases, which provides a less accurate estimate of the actual elastic modulus.

Table 1. Material properties of constituents

Material	E (GPa)	ν
Epoxy	3.5	0.33
Glass	72.3	0.22

The composition of each labeled numerical sample type is listed in table 2. The diameter of particles is evaluated at two levels ([S1, S2], [C1, C2]). S1 and S2 corresponds to a diameter of 1/6 and 1/8 of the unit cube's length while C1 and C2 corresponds to a diameter of 0.085 and 0.064 of the cube's unit length. The elongation of cylindrical particles is chosen using a ratio of length to diameter equal to five. The volume of an individual particle is the same between S1, C1 and between S2, C2. Four targets for the volume fraction of spherical particles are considered: 5% (FV5), 10% (FV10), 15% (FV15) and 20% (FV20) and two targets for the volume fractions of cylindrical particles are considered: 5% (FV5) and 10% (FV10). The volume fraction of cylindrical particles is limited to 10% because inserting a cylindrical particle is harder than inserting a spherical particle due to cylindrical particle's elongation. Higher volume fraction values could be attained by varying particles geometrical properties according to a predefined distribution rather than a fixed value. This distribution would allow the RSA algorithm to insert smaller particles in thither spaces otherwise unfilled. As mentioned previously, a rearrangement algorithm could help to increase the attainable volume fraction. Another solution could be to use a rigid

body physics engine to simulate the compaction of a high-volume fraction of particles and to generate SVEs CAD models based on rigid body physics simulation results.

Table 2. List of numerical samples

Particle	Label	Geometrical properties	$V_{f_{target}}$	$Dist_{min}$	Number of samples
Sphere	S1FV5	$Dia. = 1/6$	5%	0.04	100
	S1FV10	$Dia. = 1/6$	10%	0.04	100
	S2FV10	$Dia. = 1/8$	10%	0.04	20
	S2FV15	$Dia. = 1/8$	15%	0.02	20
	S2FV20	$Dia. = 1/8$	20%	0.01	20
Cylinder	C1FV5	$Dia. = 0.085, L/D = 5$	5%	0.03	100
	C1FV10	$Dia. = 0.085, L/D = 5$	10%	0.03	100
	C2FV10	$Dia. = 0.064, L/D = 5$	10%	0.02	20

As mentioned previously, FEA simulation for each SVE is carried out automatically and results obtained are averaged according to equations (6-7). Figure 12 illustrates stress and strain fields for case C1FV10 with a quadratic mesh under hydrostatic KUBC. Based on averaged stress and strain tensors, apparent shear G_{app} and compressibility K_{app} moduli are calculated using equations (8-9). Finally, the apparent elastic modulus E_{app} is obtained and compared with Voigt, Reuss and Hashin-Shtrikman bounds as reported in table 3. In table 3, analytic bounds are calculated according to volume fractions of particles that are evaluated from the CAD models of SVEs, which are listed in table 4. In figure 13 the elastic modulus obtained for each SVE is plotted with respect to the volume fraction of elements belonging to the particles for cases S1FV10 and C1FV10 with linear and quadratic elements. In figure 14, the elastic modulus for the S2 cases is plotted according to the volume fraction of quadratic elements. As expected, apparent elastic moduli obtained using KUBC (Kinematic Uniform Boundary Conditions) is higher than those obtained with SUBC (Static Uniform Boundary Conditions). Comparing results obtained with quadratic and linear elements has been investigated to quantify the effect of using quadratic elements. This effect is indeed twofold. First, as explained earlier, relocating middle nodes increases the volume fraction of particles which, in turn, slightly increases the modulus of elasticity. The second effect originates from the fact that linear tetrahedrons classically tends to overestimate material stiffness. The

use of quadratic elements provides a better estimation of stiffness, which accounts for the drop of the elasticity modulus. The increase in the number of particles from [S1,C1] to [S2,C2], decreases the difference between elastic moduli obtained with KUBC and SUBC, which is consistent with literature [12]. Comparing the elastic modulus obtained between samples with spherical and cylindrical particles reveals the influence of particles geometry on mechanical properties. Indeed, an increase of the elasticity modulus is observed with cylindrical particles. This is explained considering that stress transfer from particle to particle is better with cylindrical particles than with spherical particles, resulting in a stiffer composite material.
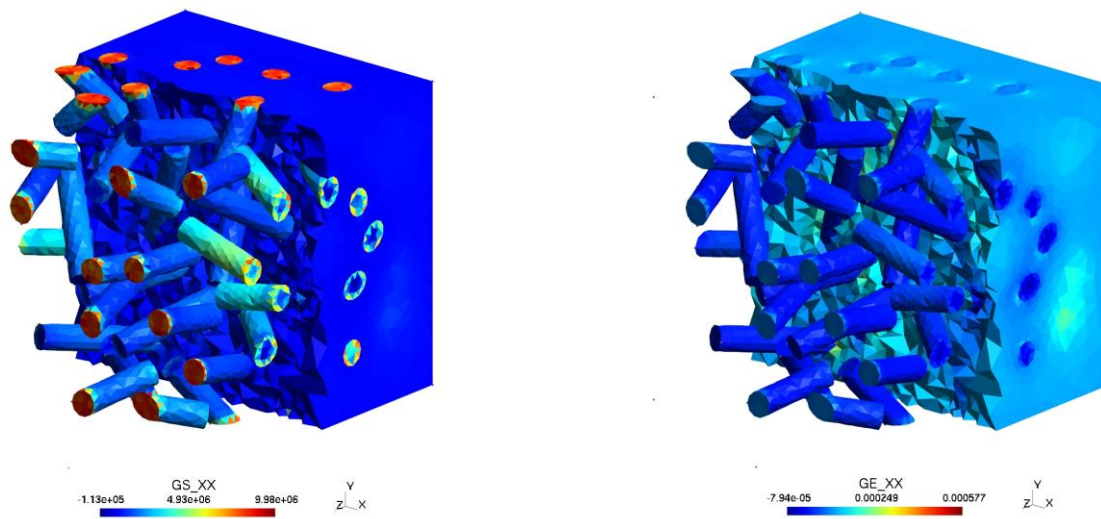

Fig. 12. Stress σ_{xx} (left) and strain ε_{xx} (right) for C1FV10 using a quadratic mesh.

Table 3. Modulus of elasticity

Label	E_{app} (GPa)							
	SUBC		KUBC		Analytic bounds			
	linear	quadratic	linear	quadratic	Reuss	HS$^-$	HS$^+$	Voigt
S1FV5	3.88 ± 0.01	3.82 ± 0.01	4.11 ± 0.05	4.02 ± 0.05	3.67	3.84	5.40	7.01
S1FV10	4.28 ± 0.01	4.17 ± 0.01	4.87 ± 0.07	4.69 ± 0.06	3.87	4.22	7.37	10.47
S2FV10	4.31 ± 0.01	4.19 ± 0.01	4.59 ± 0.03	4.42 ± 0.02	3.87	4.22	7.35	10.44
S2FV15	---	4.60 ± 0.01	---	5.04 ± 0.03	4.08	4.63	9.41	13.88
S2FV20	---	5.06 ± 0.01	---	5.76 ± 0.04	4.32	5.09	11.56	17.32
C1FV5	3.95 ± 0.02	3.90 ± 0.02	4.15 ± 0.04	4.09 ± 0.04	3.67	3.84	5.40	7.01
C1FV10	4.42 ± 0.03	4.33 ± 0.03	4.93 ± 0.05	4.80 ± 0.05	3.87	4.22	7.36	10.45
C2FV10	4.46 ± 0.02	4.35 ± 0.02	4.90 ± 0.04	4.75 ± 0.04	3.87	4.21	7.34	10.43
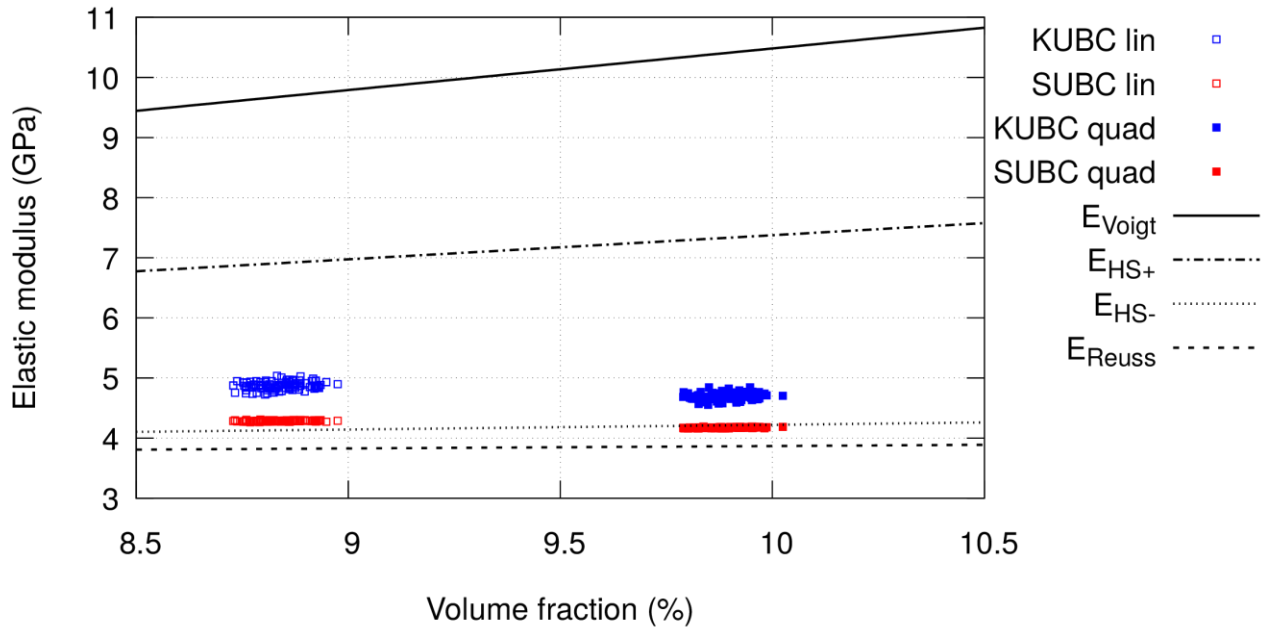
a)
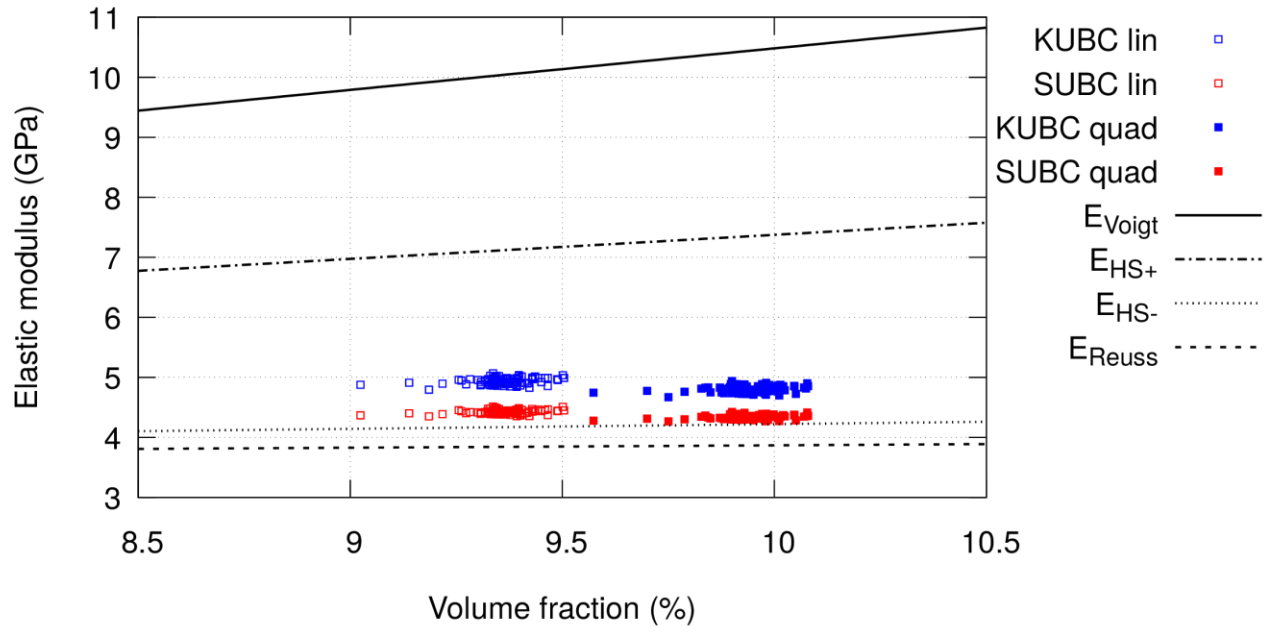
b)

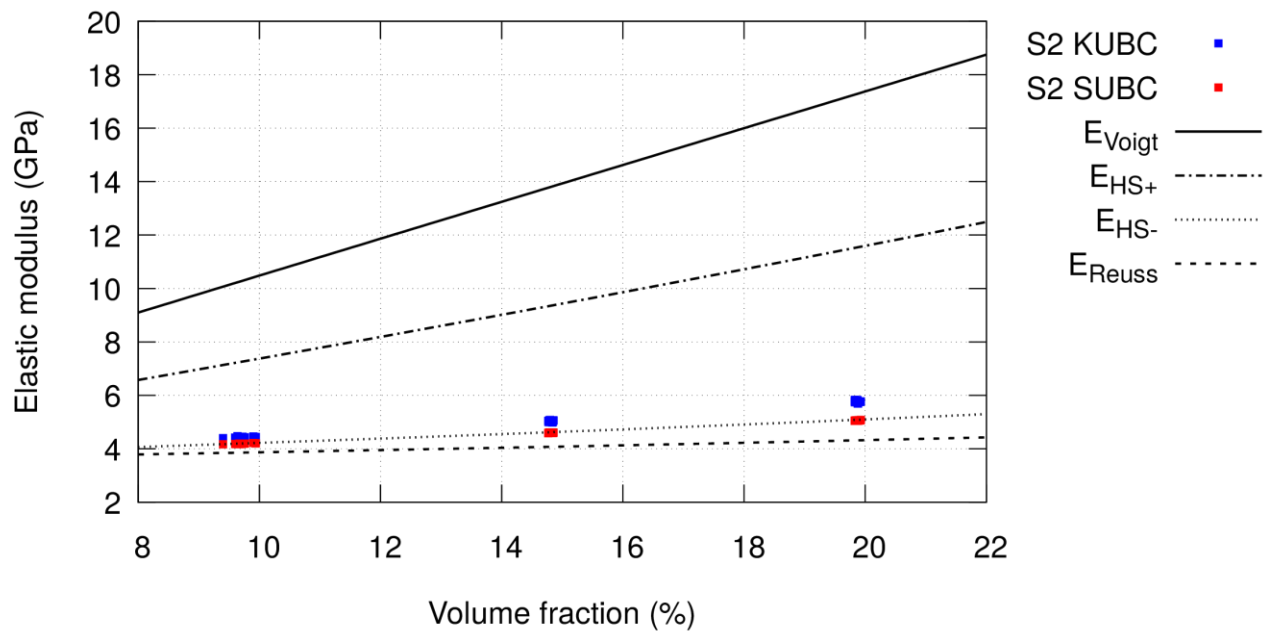Fig. 13. Modulus of elasticity scatter for S1FV10 (a) and C1FV10 (b)

Fig. 14. Modulus of elasticity scatter for S2 using quadratic elements

Mean and standard deviation values for the volume fraction, particle size and number of particles for each sample type, are reported in table 4. Mean volume fraction values obtained are very close to target volume fractions and low standard deviations obtained indicate a low scatter. As expected, to fulfill a given required volume fraction with smaller particles (S2, C2) more particles need to be generated. Although volumes of spherical and cylindrical particles are initially the same before their insertion, cylindrical particles tend to be smaller than spherical particles. This difference is caused by the elongation of cylindrical particles which, for a limited insertion volume, tend to be cut more often by boundaries of SVEs than spherical particles.

Table 4. CAD model constitution. Particle volume fraction, particle volume and number of particles.

Label	V_f (%)	Particle volume (10^{-3})	Number of particles
S1FV5	4.99 ± 0.05	2.07 ± 0.107	24 ± 1
S1FV10	9.98 ± 0.05	1.95 ± 0.071	51 ± 2
S2FV10	9.94 ± 0.09	0.996 ± 0.003	100 ± 1
S2FV15	14.93 ± 0.02	0.983 ± 0.003	152 ± 1
S2FV20	19.92 ± 0.01	0.972 ± 0.004	205 ± 1
C1FV5	4.98 ± 0.06	1.84 ± 0.096	27 ± 1
C1FV10	9.95 ± 0.07	1.62 ± 0.055	61 ± 2
C2FV10	9.92 ± 0.02	0.629 ± 0.024	158 ± 6

Locations obtained for the center of mass of SVEs are listed in table 5. The center of mass being located at the center of unit cubes and obtaining identical values for moments of inertia (not shown in Table 5) indicate that the distribution of particles is isotropic.

Table 5. Location of the center of mass in the unit cube

Label	x	y	z
S1FV5	0.502 ± 0.040	0.501 ± 0.037	0.500 ± 0.035
S1FV10	0.501 ± 0.017	0.499 ± 0.018	0.502 ± 0.019
S2FV10	0.502 ± 0.010	0.499 ± 0.010	0.500 ± 0.012
S2FV15	0.501 ± 0.008	0.503 ± 0.008	0.501 ± 0.008
S2FV20	0.502 ± 0.005	0.500 ± 0.006	0.502 ± 0.008
C1FV5	0.506 ± 0.026	0.498 ± 0.025	0.501 ± 0.028
C1FV10	0.499 ± 0.014	0.498 ± 0.012	0.499 ± 0.012
C2FV10	0.505 ± 0.010	0.507 ± 0.008	0.498 ± 0.008

For cylindrical particles (cases C1FV5, C1FV10 and C2FV10) orientation tensors obtained are listed in table 6. The fact that these tensors are very close to diagonal tensors indicates that the distribution of particles orientation is isotropic.

Table 6. Orientation tensors; C1FV5 (a), C1FV10 (b), C2FV10 (c)

a)

$$\begin{bmatrix} 0.330 & -0.004 & -0.002 \\ -0.004 & 0.338 & -0.004 \\ -0.002 & -0.004 & 0.331 \end{bmatrix}$$

b)

$$\begin{bmatrix} 0.324 & -0.002 & 0.000 \\ -0.002 & 0.333 & 0.009 \\ 0.000 & 0.009 & 0.343 \end{bmatrix}$$

c)

$$\begin{bmatrix} 0.349 & 0.007 & 0.002 \\ 0.007 & 0.322 & -0.003 \\ 0.002 & -0.003 & 0.329 \end{bmatrix}$$

Parameters of mesh size maps used are listed in table 7. Based on these parameters and for each SVE, a linear mesh is first created and based on this mesh, a quadratic mesh is generated. Therefore, both meshes (linear and quadratic) are composed of the same elements, the only difference being the presence of

middle nodes in quadratic meshes and their location on curved geometrical entities. As illustrated in figure 11, the impact of relocating middle nodes for quadratic elements in contact with curved topological entities is obvious. This impact is also illustrated in volume fraction data reported in table 8. Indeed, comparison between particle volume fractions for linear and quadratic meshes shows that the mesh volume fraction is inferior for linear meshes, due to the tessellation effect. Switching from linear to quadratic elements, the volume fraction of a SVE becomes nearly identical to the volume fraction based on the SVE CAD model, which means based on the actual geometry of inclusions. Thus, using a CAD model as original representation of the microstructure, computing a size map from this CAD model, using proven automatic CAD mesh generation algorithms and relocating middle nodes of quadratic elements provides a very accurate discretized representation of the intended microstructure.

Table 7. Size map parameters

Particle	(S1, S2)	(C1, C2)
E_n	0.08	
E_{inter}	0.04	0.02
Nb_{ele}	2	
$n_{x,y,z}$	50	
Nb_{step}	8	
f	1.25	

Table 8. Mesh data. Particle's mesh volume fractions with linear and quadratic elements, total number of elements and quality factor.

Label	V_f% linear	V_f% quadratic	Number of elements	Quality Q_K
S1FV5	4.36 ± 0.05	4.91 ± 0.05	31960 ± 1384	0.60 ± 0.002
S1FV10	8.84 ± 0.06	9.88 ± 0.05	55160 ± 1828	0.59 ± 0.002
S2FV10	8.27 ± 0.08	9.70 ± 0.12	91023 ± 2110	0.59 ± 0.001
S2FV15	---	14.8 ± 0.03	285276 ± 8463	0.63 ± 0.001
S2FV20	---	19.8 ± 0.11	504086 ± 12180	0.62 ± 0.001
C1FV5	4.68 ± 0.05	4.97 ± 0.06	116728 ± 2101	0.59 ± 0.001
C1FV10	9.36 ± 0.07	9.94 ± 0.07	213322 ± 2935	0.60 ± 0.001
C2FV10	9.05 ± 0.03	9.88 ± 0.02	344720 ± 3390	0.60 ± 0.001

The influence of the mesh size map can be observed on the number of mesh elements generated. As the volume fraction of particles increases, particles come closer to each other, which makes that the size map algorithm decreases mesh elements size in order to insure the required minimum number of elements layers between two topological entities. This mesh refinement process reduces CPU time required for the FEA simulation by allowing the generation of smaller elements where needed and coarser elements elsewhere which reduces the total number of elements if compared with a uniformly sized mesh. The number of elements is significantly higher for SVEs with cylindrical particles if compared with SVEs with spherical particles. This difference is partly due to E_{inter}, which is the mesh size imposed at the interface between particles and matrix. Indeed, E_{inter} is lower for cases with cylindrical particles to insure accurately modeling mechanical behavior at the fiber level due the elongation of fibers and due to a smaller diameter if compared to that of spherical particles. A higher number of elements for SVEs with cylindrical particles can also be explained because a lower minimum distance between two topological entities (referred to as $Dist_{min}$ in Algo 1) must be considered to reach the target volume fraction. Quality of mesh elements, as defined by Equation (5), also benefits from using automatic mesh generation procedures (in this case the advancing front mesh generation algorithm). As reported in table 8, the average quality for linear elements is high. As illustrated in figure 15, the distribution of quality is mostly centered around the average value and the percentage of elements below 0.2 is very low, with a sudden

drop under 0.2. This is due to the fact that, when possible, the mesh generation algorithm suppresses elements that are below a minimum quality threshold (in this case 0.2) and re-meshes the area.
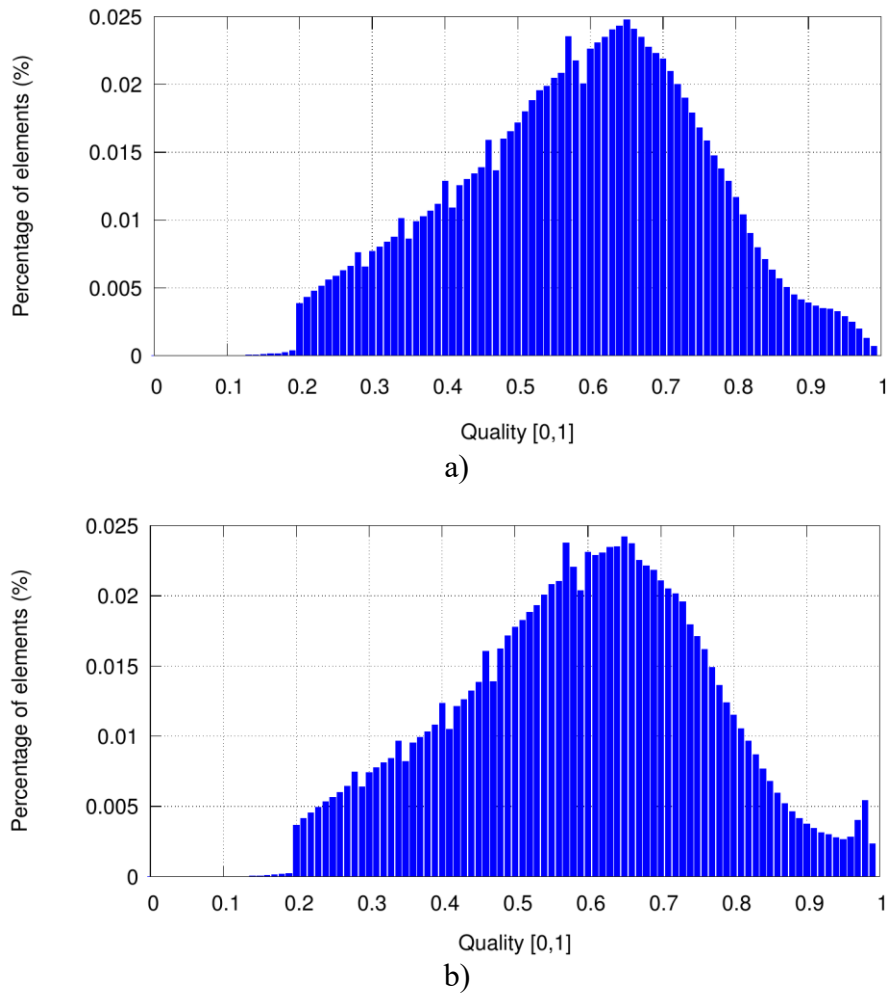

Fig. 15. Element's quality distribution for S1FV10 (a) and C1FV10 (b)

In this work, the SVE modeling approach is applied to SVEs filled with spherical and cylindrical particles. This modeling approach can easily be generalized to any shape of particles since it is based on a CAD representation of microstructures. Using CAD tools, the modified RSA algorithm is not restricted to a particular type of shape for particles. Another benefit of using a CAD representation is that mesh generation can be carried out using robust and proven CAD models automatic mesh generation algorithms. Concepts and tools underlying the UTM contribute to a complete and robust automation of the generation, simulation and post-processing of great numbers of SVEs for a wide range of particles shape.

8. Conclusion

The need to model more and more complex heterogeneous particle-based materials as led to the development of numerous SVE's representation and meshing schemes. Many of these approaches are limited to a specific geometry of particles or constrained by the use of specific mesh generation procedures, which highly limits their potential. In this work, a new methodology is proposed towards automatically generating, simulating and post-processing SVEs for particle-based materials. This methodology is mainly based on using CAD/FEA integration concepts and tools. BREP geometric modelling concepts, such as co-topology in particular, used in conjunction with a modified RSA algorithm allow the fast and efficient automatic generation of very accurate geometric representations of material microstructures. From the CAD representation of a SVE, a mesh size map can be automatically generated and used by proven and efficient automatic mesh generation algorithms to minimize the number of finite elements while preserving quality of the discretization. Quadratic elements are used to ensure accuracy of both geometric tessellation and FEA results. FEA simulation and post-processing are also carried out autonomously. An application of this methodology has been carried out on a short glass fiber / epoxy matrix material to illustrate the potential of this new approach. The effects of the particle's shape, of the curved quadratic finite elements and of the boundary conditions on the elastic modulus have been highlighted to emphasise the benefits of this methodology.

Full automation, accuracy of generated geometrical models, quality of derived FEA meshes and FEA solutions and versatility of the approach with respect to the shape of particles considered are the most interesting and promising aspects of this methodology. Extending this methodology to other types of materials, to other types and shapes of particles, to other spatial distributions of particles and to other types of behavior (non-linear mechanics heat transfer, etc.) can be easily foreseen.

References

1. Di Paola, F., *Multi-scale modeling of the thermo-mechanical behavior of particle-based composites*. 2010, Ecole Centrale Paris.
2. Böhm, H.J., A. Eckschlager, and W. Han, *Multi-inclusion unit cell models for metal matrix composites with randomly oriented discontinuous reinforcements.* Computational Materials Science, 2002. **25**(1): p. 42 - 53.
3. Rasool, A. and H.J. Böhm, *Effects of particle shape on the macroscopic and microscopic linear behaviors of particle reinforced composites.* International Journal of Engineering Science, 2012. **58**: p. 21 - 34.
4. Moumen, A.E., et al., *Effect of reinforcement shape on physical properties and representative volume element of particles-reinforced composites: Statistical and numerical approaches.* Mechanics of Materials, 2015. **83**: p. 1 - 16.
5. Böhm, H.J. and A. Rasool, *Effects of particle shape on the thermoelastoplastic behavior of particle reinforced composites.* International Journal of Solids and Structures, 2016. **87**: p. 90 - 101.
6. Ganesh, V.V. and N. Chawla, *Effect of particle orientation anisotropy on the tensile behavior of metal matrix composites: experiments and microstructure-based simulation.* Materials Science and Engineering: A, 2005. **391**(1): p. 342 - 353.
7. Hua, Y. and L. Gu, *Prediction of the thermomechanical behavior of particle-reinforced metal matrix composites.* Composites Part B: Engineering, 2013. **45**(1): p. 1464 - 1470.
8. Kari, S., et al., *Computational evaluation of effective material properties of composites reinforced by randomly distributed spherical particles.* Composite Structures, 2007. **77**(2): p. 223 - 231.
9. Segurado, J. and J. LLorca, *Computational micromechanics of composites: The effect of particle spatial distribution.* Mechanics of Materials, 2006. **38**(8): p. 873 - 883.
10. Segurado, J., C. González, and J. LLorca, *A numerical investigation of the effect of particle clustering on the mechanical properties of composites.* Acta Materialia, 2003. **51**(8): p. 2355 - 2369.
11. Gusev, A.A., *Representative volume element size for elastic composites: A numerical study.* Journal of the Mechanics and Physics of Solids, 1997. **45**(9): p. 1449 - 1459.
12. Kanit, T., et al., *Determination of the size of the representative volume element for random composites: statistical and numerical approach.* International Journal of Solids and Structures, 2003. **40**(13): p. 3647 - 3679.
13. Khisaeva, Z.F. and M. Ostoja-Starzewski, *On the Size of RVE in Finite Elasticity of Random Composites.* Journal of Elasticity, 2006. **85**(2): p. 153.
14. Gitman, I.M., H. Askes, and L.J. Sluys, *Representative volume: Existence and size determination.* Engineering Fracture Mechanics, 2007. **74**(16): p. 2518 - 2534.
15. Kari, S., H. Berger, and U. Gabbert, *Numerical evaluation of effective material properties of randomly distributed short cylindrical fibre composites.* Computational Materials Science, 2007. **39**(1): p. 198 - 204.
16. Harper, L.T., et al., *Representative volume elements for discontinuous carbon fibre composites – Part 2: Determining the critical size.* Composites Science and Technology, 2012. **72**(2): p. 204 - 210.
17. Dirrenberger, J., S. Forest, and D. Jeulin, *Towards gigantic RVE sizes for 3D stochastic fibrous networks.* International Journal of Solids and Structures, 2014. **51**(2): p. 359 - 376.

18. Ferrié, E., et al., *Fatigue crack propagation: In situ visualization using X-ray microtomography and 3D simulation using the extended finite element method.* Acta Materialia, 2006. **54**(4): p. 1111 - 1122.

19. Coleri, E., et al., *Development of a micromechanical finite element model from computed tomography images for shear modulus simulation of asphalt mixtures.* Construction and Building Materials, 2012. **30**: p. 783 - 793.

20. Huang, M. and Y.-m. Li, *X-ray tomography image-based reconstruction of microstructural finite element mesh models for heterogeneous materials.* Computational Materials Science, 2013. **67**: p. 63 - 72.

21. Suuronen, J.-P., et al., *Analysis of short fibres orientation in steel fibre-reinforced concrete (SFRC) by X-ray tomography.* Journal of Materials Science, 2013. **48**(3): p. 1358–1367.

22. Segurado, J. and J. Llorca, *A numerical approximation to the elastic properties of sphere-reinforced composites.* Journal of the Mechanics and Physics of Solids, 2002. **50**(10): p. 2107 - 2121.

23. Brassart, L., I. Doghri, and L. Delannay, *Homogenization of elasto-plastic composites coupled with a nonlinear finite element analysis of the equivalent inclusion problem.* International Journal of Solids and Structures, 2010. **47**(5): p. 716 - 729.

24. Bailakanavar, M., et al., *Automated modeling of random inclusion composites.* Engineering with Computers, 2014. **30**(4): p. 609–625.

25. Schneider, K., B. Klusemann, and S. Bargmann, *Automatic three-dimensional geometry and mesh generation of periodic representative volume elements for matrix-inclusion composites.* Advances in Engineering Software, 2016. **99**: p. 177 - 188.

26. Wang, W., et al., *Micromechanical Modeling of Fiber-Reinforced Composites with Statistically Equivalent Random Fiber Distribution.* Materials, 2016. **9**(8).

27. Ogierman, W. and G. Kokot, *Generation of the representative volume elements of composite materials with misaligned inclusions.* Composite Structures, 2018. **201**: p. 636 - 646.

28. Pan, Y., L. Iorga, and A.A. Pelegri, *Analysis of 3D random chopped fiber reinforced composites using FEM and random sequential adsorption.* Computational Materials Science, 2008. **43**(3): p. 450 - 461.

29. Pan, Y., L. Iorga, and A.A. Pelegri, *Numerical generation of a random chopped fiber composite RVE and its elastic properties.* Composites Science and Technology, 2008. **68**(13): p. 2792 - 2798.

30. Lu, Z., Z. Yuan, and Q. Liu, *3D numerical simulation for the elastic properties of random fiber composites with a wide range of fiber aspect ratios.* Computational Materials Science, 2014. **90**: p. 123 - 129.

31. Tian, W., et al., *Representative volume element for composites reinforced by spatially randomly distributed discontinuous fibers and its applications.* Composite Structures, 2015. **131**: p. 366 - 373.

32. Ghossein, E. and M. Lévesque, *A fully automated numerical tool for a comprehensive validation of homogenization models and its application to spherical particles reinforced composites.* International Journal of Solids and Structures, 2012. **49**(11): p. 1387 - 1398.

33. Ghossein, E. and M. Lévesque, *Random generation of periodic hard ellipsoids based on molecular dynamics: A computationally-efficient algorithm.* Journal of Computational Physics, 2013. **253**: p. 471 - 490.

34. Li, G., et al., *A new approach to rapidly generate random periodic representative volume elements for microstructural assessment of high volume fraction composites.* Materials & Design, 2018. **150**: p. 124 - 138.

35. Frey, P.J. and P.-L. George, *Mesh Generation: Application to Finite Elements*. 2007: ISTE.

36.   Owen, S.J., et al., *Hexahedral Mesh Generation for Computational Materials Modeling.* Procedia Engineering, 2017. **203**: p. 167 - 179.

37.   Cuillière, J.-C. and V. Francois, *Integration of CAD, FEA and Topology Optimization through a Unified Topological Model.* Computer-Aided Design and Applications, 2014. **11**(5): p. 493-508.

38.   Cuillière, J.-C., V. François, and A. Nana, *Automatic construction of structural CAD models from 3D topology optimization.* Computer-Aided Design and Applications, 2018. **15**(1): p. 107-121.

39.   Sattarpanah Karganroudi, S., et al., *"What-if" scenarios towards virtual assembly-state mounting for non-rigid parts inspection using permissible loads.* The International Journal of Advanced Manufacturing Technology, 2018. **97**(1): p. 353–373.

40.   Cuillière, J.-C., V. François, and R. Lacroix, *A new approach to automatic and a priori mesh adaptation around circular holes for finite element analysis.* Computer-Aided Design, 2016. **77**: p. 18 - 45.

41.   Open Cascade S.A.S, *Open Cascade Technology*. 2018: Open source on www.opencascade.com.

42.   Advani, S.G. and C.L. Tucker, *The Use of Tensors to Describe and Predict Fiber Orientation in Short Fiber Composites.* Journal of Rheology, 1987. **31**(8): p. 751-784.

43.   Cuillière, J.C., *A direct method for the automatic discretization of 3D parametric curves.* Computer-Aided Design, 1997. **29**(9): p. 639 - 647.

44.   Cuillière, J.C., *An adaptive method for the automatic triangulation of 3D parametric surfaces.* Computer-Aided Design, 1998. **30**(2): p. 139 - 149.

45.   Turner, M., J. Peiró, and D. Moxey, *Curvilinear mesh generation using a variational framework.* Computer-Aided Design, 2018. **103**: p. 73 - 91.

46.   Johnen, A., et al., *Efficient Computation of the Minimum of Shape Quality Measures on Curvilinear Finite Elements.* Procedia Engineering, 2016. **163**: p. 328 - 339.

47.   Toulorge, T., et al., *Robust untangling of curvilinear meshes.* Journal of Computational Physics, 2013. **254**: p. 8 - 26.

48.   Électricité de France, *Code_Aster, Analysis of Structures and Thermomechanics for Studies & Research*. 2019: Open source on www.code-aster.org.

49.   Voigt, W., *Ueber die Beziehung zwischen den beiden Elasticitätsconstanten isotroper Körper.* Annalen der Physik, 1889. **274**(12): p. 573-587.

50.   Reuss, A., *Berechnung der Fließgrenze von Mischkristallen auf Grund der Plastizitätsbedingung für Einkristalle.* ZAMM - Journal of Applied Mathematics and Mechanics / Zeitschrift für Angewandte Mathematik und Mechanik, 1929. **9**(1): p. 49-58.

51.   Hashin, Z. and S. Shtrikman, *A variational approach to the theory of the elastic behaviour of multiphase materials.* Journal of the Mechanics and Physics of Solids, 1963. **11**(2): p. 127-140.